Structure and Phase Diagram of Nucleosome Core Particles Aggregated by Multivalent Cations

Aurélie Bertin,* Stéphanie Mangenot,* Madalena Renouard,* Dominique Durand,† and Françoise Livolant*
*Laboratoire de Physique des Solides, CNRS UMR 8502, and †Institute de Biochemie, Biophysique Moléculaire et Cellulaire (IBBMC), CNRS UMR 8619, Université Orsay-Sud, Paris, France

ABSTRACT The degree of compaction of the eukaryotic chromatin in vivo and in vitro is highly sensitive to the ionic environment. We address the question of the effect of multivalent ions on the interactions and mutual organization of the chromatin structural units, the nucleosome core particles (NCPs). Conditions of precipitation of NCPs in the presence of 10 mM Tris buffer and various amounts of either magnesium (Mg^{2+}) or spermidine (Spd^{3+}) are explored, compared, and discussed in relation to theoretical models. In addition, the structure of the aggregates is analyzed by complementary techniques: freeze-fracture electron microscopy, cryoelectron microscopy, and x-ray diffraction. In Mg^{2+}-NCP aggregates, NCPs tend to stack on top of one another to form columns that are not long-range organized. In the presence of Spd^{3+}, NCPs precipitate to form a dense isotropic phase, a disordered phase of columns, a two-dimensional columnar hexagonal phase, or a three-dimensional crystal. The more ordered phases (two-dimensional or three-dimensional hexagonal) are found close to the precipitation line, where the number of positive charges carried by cations is slightly larger than the number of available negative charges of the NCPs. All ordered phases coexist with the dense isotropic phases. Formation of hexagonal and columnar phases is prevented by an excess of polycations.

INTRODUCTION

Nucleosome core particles (NCPs) are made up of 146–147 DNA basepairs wrapped around a histone octamer in a left-handed superhelix. Their structure has been determined by x-ray crystallography at a resolution of 1.9 Å (1,2). A twofold axis of symmetry (the dyad axis) is perpendicular to the superhelix axis of the particle. NCPs are colloidal particles 11 nm wide and 6 nm thick. They carry a net structural charge of −150, with a heterogeneous distribution of positive and negative charges. Negative DNA phosphate groups are located at the periphery of the NCP. Positive charges are essentially located on the histone flexible tails that may extend outside of the particle and represent ~30% of the protein amino acids. These tails are positively charged due to their high content of lysine and arginine residues. NCPs are stable, with no dissociation of DNA from the protein core under a defined range of conditions that can be controlled experimentally. Being monodisperse in size, charge, and shape, NCPs constitute an interesting model by which to study colloidal solutions.

In fact, phase diagrams of colloids have been studied for almost a century because of their high theoretical interest and also because of potential industrial applications. Upon a change in the quality of the solvent, driven by temperature or changes in ionic conditions, aggregates of a dense phase may form. Depending on their size and density, these aggregates may stay in suspension, coalesce, or phase-separate from the dilute solution. Over the last years, microaggregation occurring in solutions of charged particles has attracted much attention from theorists and experimentalists (for a review, see de Vries and Stuart (3) and references therein). There is also a growing interest in colloids with anisotropic shapes (4) and surface-charge heterogeneities (5). NCPs, with their $L/D = 0.5$ ratio, their back and front sides (determined by the dyad axis), their inhomogeneous distribution of charges, and their chiral properties, provide a richness of interaction that can be monitored by varying the volume fraction of the particles and the ionic conditions (mono-, di-, and multivalent cations). Also, very little attention has been devoted to the structure of colloidal aggregates, with a few exceptions (6). This is another aspect that we can address using NCPs.

On the other hand, solutions of isolated NCP constitute also a simplified model of chromatin organization. Because of the absence of high-resolution methods that would be powerful enough to resolve the highly complex, dense, and heterogeneous local structure of chromatin inside the cell nucleus, we still don't know how the chain of nucleosomes is packed locally along active and inactive parts of the genome, and we are yet unable to understand how transitions occur between these states. Compared to long chromatin fragments, isolated NCPs organize faster and over larger distances, thus providing easier access for structural investigation. Structures formed by these isolated particles do not necessarily reproduce the structures of native chromatin, but they provide information on the way nucleosomes interact with each other depending on the ionic conditions (which can be precisely controlled and varied) in the absence of topological constraints introduced by the linker DNA that connects nucleosomes in vivo. We have already explored the structures formed by isolated NCPs in the presence of monovalent cations, over a physiological range of NCP concentrations (50–250 mg/ml) (7,8). We focus here on the effects of magnesium and

Submitted March 7, 2007, and accepted for publication July 20, 2007.

Address reprint requests to Stéphanie Mangenot, Laboratoire de Physique des Solides, CNRS UMR 8502, Université Paris-Sud, 91405 Orsay cedex, France. E-mail: mangenot@lps.u-psud.fr.

Editor: Tamar Schlick.

0006-3495/07/11/3652/12 $2.00
doi: 10.1529/biophysj.107.108365

spermidine, which are divalent and trivalent cations, respectively. Contrary to monovalent ions, cations of valence 2 and higher have been shown to condense isolated chromosomes (9), chromatin chains (10), and NCPs (11) but have no condensing effect on linear DNA (12). Both cations were chosen because of their high importance in the activity of chromatin. Magnesium is a cofactor essential to the activity of numerous enzymes involved in replication, transcription, and recombination. Polyamines are low-molecular-weight polycations involved in cellular differentiation and growth (13). Among them, spermidine is the most abundant in eukaryotic cells (14). Concentrations of these cations in living cells cannot be determined with high precision, because they are difficult to measure precisely and also because they may be inhomogeneously distributed inside the cells and vary with the cell type under consideration. Estimations can be given anyway. Magnesium is particularly abundant within mitotic chromosomes (17 mM), as compared with interphase chromatin (3 mM) (15). The concentration of spermidine reaches several millimolars. Polyamines are mostly bound to negatively charged cellular components (DNA, RNA, acidic proteins, etc.) and only 7–15% are free in solution (16).

A previous study considering the precipitation of NCPs by magnesium (11) disregarded the structural aggregates feature. On the other hand, using spermidine, Leforestier et al. (17) concentrated on structural issues without fully determining the precipitation conditions. We propose here to give a complete overview of both the precipitation conditions and the structure of the aggregates, upon precipitation with spermidine and magnesium. Phase diagrams will be completely described and theoretical models will be discussed. The effect of cation valence will also be discussed. Aggregate structures will be determined by appropriate methods and the structural features will be located in the phase diagrams.

MATERIAL AND METHODS

Nucleosome core particle preparation

Nucleosome core particles (NCPs) were prepared from H1-depleted calf thymus chromatin as described by Mangenot et al. (18). More precisely, several grams of NCPs were obtained after controlled micrococcal nuclease (Amersham Bioscience) digestion of chromatin. After suspension in 150 mM NaCl (Sigma, St. Louis, MO), 1 mM EDTA (ethylenediaminetetraacetic acid) (Sigma), 10 mM Tris-HCl (Sigma), pH 7.6, NCPs were purified by chromatography using Sephacryl S300 HR (Amersham Bioscience). Nondenaturing 5% polyacrylamide electrophoresis gels were used to control the absence of both free DNA and polynucleosomes. The composition and integrity of histones were checked on 15% polyacrylamide electrophoresis gels. The length of DNA associated with the histone octamer was assessed at 155 ± 20 basepairs by electrophoresis on 12% polyacrylamide gels. To remove any EDTA traces, NCPs were dialyzed at 2 mg mL^{-1} against large volumes of 10 mM Tris-HCl, pH 7.6. Dialysis baths were changed every day for 1 week. NCPs were concentrated using centrifugal ultrafiltration devices (Vivaspin, Vivascience, Hannover, Germany) with a cut-off of molecular mass 10,000 Da. NCP concentrations were measured and adjusted using ultraviolet absorbance measurements at 260 nm ($A_{260nm} = 9.5\ cm^2\ mg^{-1}$). Experiments using either Spd^{3+} or Mg^{2+} were performed using two batches of NCPs with similar length and polydispersity of DNA, purified from distinct calf thymus.

Precipitation curves and phase diagrams

Phase diagrams were explored by varying the NCP and polycation concentrations. In this article, ''starting concentrations'' will refer to the concentrations in the sample after mixing NCP and polycation solutions. The starting concentrations ranged from 0.2 to 300 mg mL^{-1} for NCPs, from 2 to 380 mM for magnesium, and from 0.1 to 80 mM for spermidine. In conditions where precipitation occurs, the NCP concentration in the aggregate state will be called ''precipitated NCP'' concentration. We did not determine the concentration of polycations in the precipitate and the supernatant.

Two experimental procedures were used to build the phase diagrams. For starting NCP concentrations <60 mg mL^{-1}, precipitation curves were established. NCP, magnesium, and spermidine solutions were prepared in 10 mM Tris-HCl buffer, pH 7.6. An adequate volume of $MgCl_2$ (magnesium chloride hexahydrate, Sigma) or $SpdCl_3$ (Fluka, Buchs, Switzerland) solution was added to the NCPs. For a given precipitation curve, the starting NCP concentration was kept constant while magnesium or spermidine concentrations were varied. After being vortexed during a few tens of seconds, samples were centrifuged for 20 min at 11,000 × g. For each experimental point, the fraction of NCPs remaining in the supernatant was determined by ultraviolet absorbance measurement at 260 nm. Typical precipitation curves are displayed in Fig. 1. Precipitation and redissolution thresholds were graphically determined from such curves.

For starting NCP concentrations >60 mg mL^{-1}, precipitation and redissolution thresholds were determined by visual inspection, looking for sample turbidity after adding multivalent cations to NCP solutions.

The integrity of NCPs with various amounts of magnesium and spermidine ranging from a few to 300 mM and 100 mM, respectively, was checked with 5% polyacrylamide electrophoresis gels.

Optical microscopy

Samples were analyzed by optical microscopy using a microscope (Optiphot X Pol, Nikon, Tokyo, Japan) equipped for both polarizing and differential interferential Nomarski contrast imaging. After adding multivalent cations to the NCP solution, samples were inserted into flat capillaries (microslide 0.1 mm × 1 mm × 100 mm, Vitrodynamics, Rockaway, NJ). Images were recorded using a digital camera (Coolpix 8400, Nikon).

Freeze-fracture electron microscopy

Aliquots of the precipitated phases were drawn out and quickly frozen at liquid helium temperature using a slam freezing device (Cryovacublock, Reichert, Thane, India). Vitrified samples were then freeze-fractured at −150°C, shadowed at 45° with platinum, and carbonated (BAF 400T, Balzers, Balzers, Liechtenstein). After removal of any biological material by immersion in bleach and water and recovery on a microscopy grid, replicas were analyzed using an electron microscope (2011 LaB6, JEOL, Tokyo, Japan). Images were recorded with a 30,000× magnification and developed on S0-163 films (Kodak, Rochester, NY) before digitization (film scanner Supercoolscan 8000 ED, Nikon).

Cryoelectron microscopy

Mg^{2+}-NCP microaggregates were analyzed in thin vitrified films by cryoelectron microscopy. A 4-μL sample drop of the mixed sample was deposited on holey carbonated microscopy grids. After removing solution in excess, thin films of the solution (40–100 nm) were kept within holes and vitrified in liquid ethane cooled down to liquid nitrogen temperature. Vitrification was performed in a home-made controlled environment chamber where both temperature and humidity rates are imposed and controlled (to be

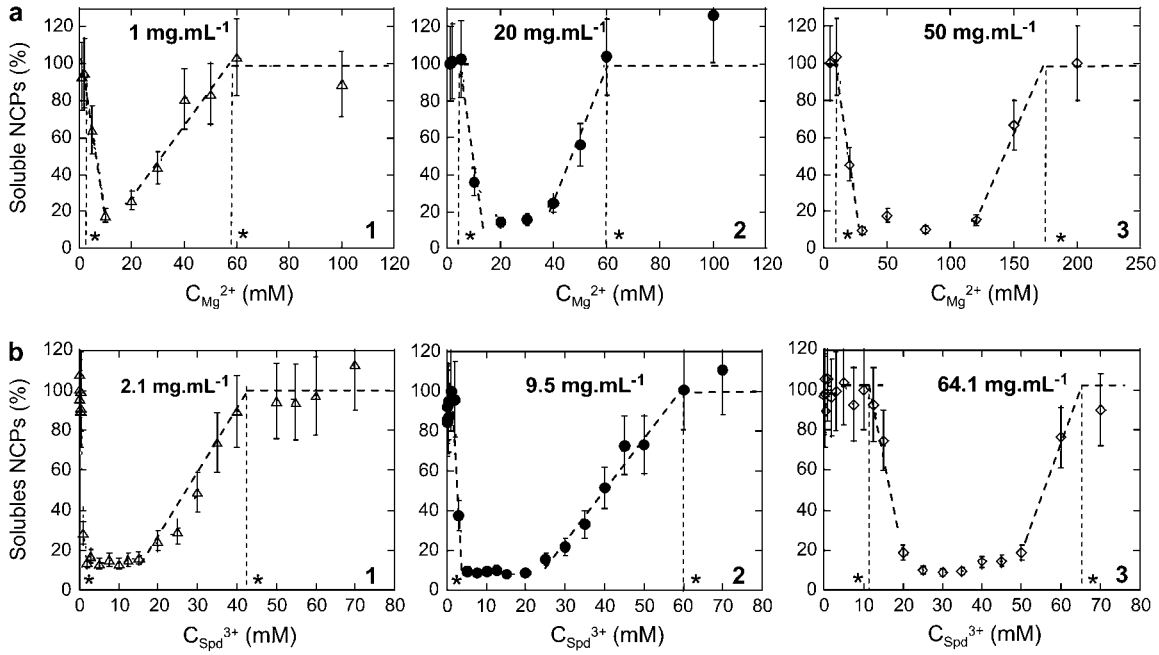

FIGURE 1 (*a*) Curves describing NCP precipitation by magnesium for starting NCP concentrations of 1 mg mL^{-1} (*1*), 20 mg mL^{-1} (*2*), and 50 mg mL^{-1} (*3*) in the presence of 10 mM Tris-HCl, pH 7.6. Threshold concentrations for precipitation and redissolution were graphically determined and are indicated here by asterisks. (*b*) Curves describing NCP precipitation by spermidine for starting NCP concentrations of 2.1 mg mL^{-1} (*1*), 9.5 mg mL^{-1} (*2*), and 64.1 mg mL^{-1} (*3*) in the presence of 10 mM Tris-HCl, pH 7.6.

published). Consequently, during the time between blotting of the sample and immersion of the thin film in ethane, evaporation was prevented and the sample ionic environment was kept unchanged. Electron micrographs were taken at liquid nitrogen temperature using a sample cryoholder (Gatan, Pleasanton, CA) with an electron microscope (2011 LaB6, JEOL) under low electron dose conditions. Pictures were taken with a 50,000× magnification, with a defocus of 1,300 nm. Images developed on S0-163 films (Kodak) were digitized using a film scanner (Supercoolscan 8000 ED, Nikon) and processed for contrast enhancement using Image J software.

X-ray diffraction

Vortexed samples were inserted into cylindrical quartz capillaries 1.5 mm in diameter (Glastechnik, Wien, Austria) and centrifuged at 1500 × *g* for a few minutes. The precipitated phase drops to the bottom of the capillaries and is kept in equilibrium with the supernatant. Full capillaries were then sealed with paraffin and equilibrated at room temperature either 1 month or 1 year before analysis. Capillaries were prepared for varying magnesium amounts, with starting NCP concentrations of 10, 50, and 100 mg mL^{-1}. A systematic x-ray study was undertaken with Spd-NCP aggregates. For starting NCP concentrations of 6, 14, 25, 30, 40, 60, 100, 150, 200, and 240 mg mL^{-1}, various Spd^{3+} concentrations were tested to investigate the entire phase diagram.

X-ray diffraction experiments were carried out at the ESRF (European Synchrotron Radiation Facility, Grenoble, France) on the ID2 beamline. The beamline wavelength was equal to 1 Å. The beam dimensions were limited to 200 × 200 μm^2, using slits. The sample-to-detector distance was set at 2 m. The diffracted signal was detected by a 1024 × 1024-pixel CCD camera. For several samples, a thermostated sample holder was used to control the temperature. First, capillaries were scanned every 0.25 mm for 0.02 s to locate the best-organized regions within the precipitate. Once such a region was found, measurement was repeated five times during 0.2 s. Care was taken to avoid x-ray damage.

RESULTS

Precipitation conditions: phase diagrams

Precipitation curves obtained for starting NCP concentrations below 60 mg mL^{-1} are displayed in Fig. 1, *a* and *b*, for Mg^{2+} and Spd^{3+}, respectively. For both cations, precipitation curves look similar. NCPs aggregate above a given concentration of cations. With increasing multivalent cation concentrations, the fraction of precipitated NCPs increases to a maximum. At that point, a rather small NCP fraction (10–20%) remains soluble, regardless of the precipitating agent (magnesium or spermidine). For higher cation concentrations, the fraction of precipitated NCPs decreases. Both precipitation and redissolution thresholds are defined graphically (Fig. 1, *asterisks*). These two values are shifted toward higher multivalent concentrations of cations with increasing starting NCP concentrations.

The resulting phase diagrams are presented in Fig. 2, *a* and *b*. Domains of aggregated NCPs are distinguished from domains where NCPs are soluble. For both phase diagrams, the quantity of charges introduced by the added multivalent cations ($Z_{multi}C_{multi}$) is plotted as a function of the apparent quantity of negative charges on NCPs (C_{ap}). For magnesium and spermidine, $Z_{multi}C_{multi}$ are respectively equal to $2C_{Mg}^{2+}$ and $3C_{Sp}^{3+}$ (mM). C_{ap} is calculated from the available negative charges carried by NCPs. Naked 155-bp DNA carries 310 negative charges, which are partially neutralized

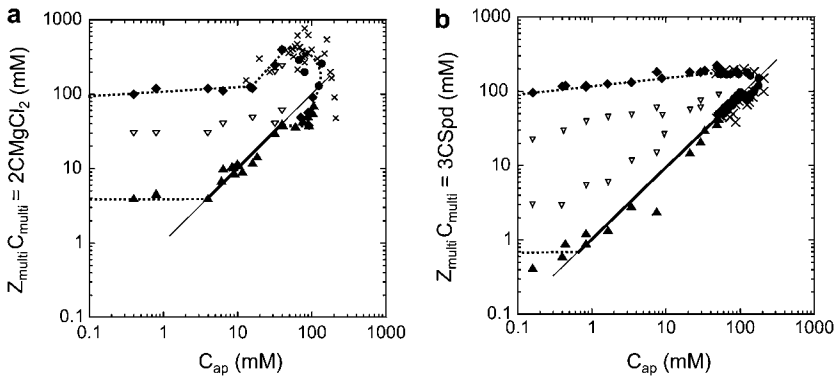

FIGURE 2 Phase diagrams of NCPs precipitated with magnesium (*a*) and spermidine (*b*) in the presence of 10 mM Tris-HCl. They display $Z_{multi}C_{multi} = 2C_{Mg}^{2+}$ or $Z_{multi}C_{multi} = 3C_{Spd}^{3+}$ as a function of C_{ap} (mM) = $0.799C_{NCPs}$ (mg mL^{-1}). The positive charge amounts carried by magnesium or spermidine are plotted as a function of the negative charge amounts available on the NCPs. The equations $Z_{multi}C_{multi} = C_{ap}$ are indicated by continuous lines. Dashed lines serve as a guide for the eye. Precipitation (▲) and redissolution (♦) points obtained from the precipitation curves are indicated. Above 60 mg mL^{-1} (C_{ap} = 47.8 mM), the solution state was determined by visual inspection before centrifugation and was either turbid (●) or transparent (×).

by the histone octamer, which carries 214 positive and 72 negatives charges. There are 168 negative charges still accessible for interaction with cations. Taking the DNA/histone mass ratio into consideration, C_{ap} (mM) therefore equals 0.799 C_{NCPs} (mg mL^{-1}).

The precipitation threshold depends on the NCP concentration and displays three regimes characteristic of electrostatic interactions resulting from the condensation of counterions (19,20):

1. For the lowest NCP concentrations, $C_{ap} < 5$ mM for magnesium and $C_{ap} < 1$ mM for spermidine, the precipitation threshold stays nearly constant and occurs for $Z_{multi}C_{multi} = 4$ mM and 0.6 mM for Mg^{2+} and Spd^{3+}, respectively. In this regime, the precipitation threshold (C_{precip}) is above the electroneutrality line for both cations ($Z_{multi}C_{precip} > C_{ap}$).
2. For intermediate C_{ap} (5 mM $< C_{ap} <$ 40 mM for magnesium and 1 mM $< C_{ap} <$ 90 mM for spermidine), the precipitation line is nearly superimposed on the electroneutrality line ($Z_{multi}C_{multi} = C_{ap}$). Precipitation occurs when the number of positive charges provided by the cations is roughly equal to the negative charges available on NCPs.
3. For high NCP concentrations, $C_{ap} > 40$ mM for magnesium and 90 mM for spermidine, the precipitation line deviates from the electroneutrality line. In this regime, $Z_{multi}C_{precip} < C_{ap}$.

For NCPs precipitated with magnesium, the redissolution threshold varies very slowly, up to $C_{ap} = 15$ mM. It further increases sharply above $C_{ap} = 15$ mM. In contrast, for NCPs precipitated with spermidine, the redissolution threshold only displays a slight monotonic increase.

The regions of high NCP and multivalent ion concentrations were carefully explored. At the highest cation and NCP concentrations, NCPs remain soluble. The region of NCP aggregation is apparently closed to whatever the condensing agent is.

The concentrations of cations that induce maximum precipitation of NCPs are also plotted in Fig. 2. Different features are observed depending on the precipitation agent. For $C_{ap} < 40$ mM, the maximum of precipitation occurs for one defined magnesium concentration. For higher NCP concentrations, the precipitation is at a maximum over a large magnesium-concentration range, and the limits of maximum precipitation are nearly superimposed on the precipitation and redissolution lines. On the other hand, the range of spermidine concentrations inducing the maximum of precipitation is large for low NCP concentrations and is progressively reduced as C_{ap} increases up to a well-defined value for the highest NCP concentration studied, $C_{ap} = 60$ mM.

Structure of NCP aggregates

The nature of the precipitates was analyzed for >50 experimental conditions within both phase diagrams, combining optical and electron microscopy and x-ray diffraction approaches.

Mg^{2+}-NCP aggregates

Mg^{2+}-NCP aggregates are macroscopically observed by optical microscopy and freeze-fracture electron microscopy (Fig. 3). A phase separation is visible after centrifugation, clearly discriminating a low-density supernatant phase (S) from a denser precipitate (P). Droplets originating from the supernatant phase, varying in diameter from 2 to 20 μm, remain visible in the dense phase (Fig. 3 *a*, *arrowhead*). Droplets from the dense phase are still visible in the supernatant as well, even after 20 min of centrifugation at 4000 × *g* (Fig. 3 *a*, *arrow*). The size and density of droplets seem to be affected and controlled by temperature. No long-range ordering of NCPs is detected in the aggregates by freeze-fracture electron microscopy, in agreement with findings using polarizing microscopy (samples are not birefringent).

Higher-resolution studies of NCP aggregates were performed by cryoelectron microscopy and x-ray diffraction. Cryoelectron microscopy of thin vitrified films appears to be more adapted to the lowest NCP starting concentrations (<1

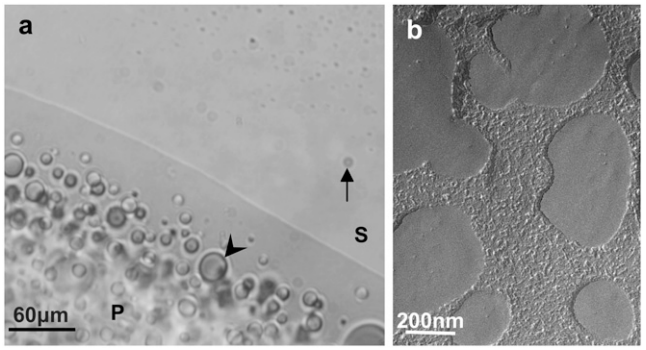

FIGURE 3 Macroscopic phase separation of NCPs (10 mg mL^{-1} starting concentration) aggregated by magnesium (20 mM) in the presence of Tris-HCl 10mM, pH 7.6. The phase separation between the supernatant (S) and the precipitated phase (P) was examined by optical microscopy (*a*) and freeze-fracture electron microscopy (*b*). The arrow indicates a droplet of the precipitate suspended in the supernatant. Droplets of the supernatant are seen in the precipitate as well (*arrowhead*).

mg mL^{-1}). The method consists of trapping small aggregates in the thickness of a thin film of solvent that is vitrified at low temperature and to analyze the local organization of NCP. Large aggregates formed at high starting NCP concentrations are too thick to be analyzed by this method.

Fig. 4, *a* and *b*, are electron micrographs of Mg^{2+}-NCP microaggregates. Since electron density is higher for DNA than for proteins, much of the contrast of NCPs originates from nucleic acids. NCPs are mainly visible by side view. They tend to pile up on top of one another and form short columns made of ~5–10 particles (Fig. 4, *a* and *b*, *arrows*) that are lying in the film. Along the columns, NCPs expose different side views, with DNA drawing a ''V'', double lines, or more complex patterns (Fig. 4 *b*). NCPs are therefore randomly oriented inside columns. Similar disordered columns were seen in the presence of monovalent ions only (17). Short columns may be aligned locally, but they do not present long-range ordering. Fourier transforms of micrographs exhibit a periodic repetitive distance of 25.8 Å, which certainly corresponds to the DNA helical pitch around the histone octamer (Fig. 4 *b*). Interparticle distances, assessed directly on micrographs, were, on average, 58 Å.

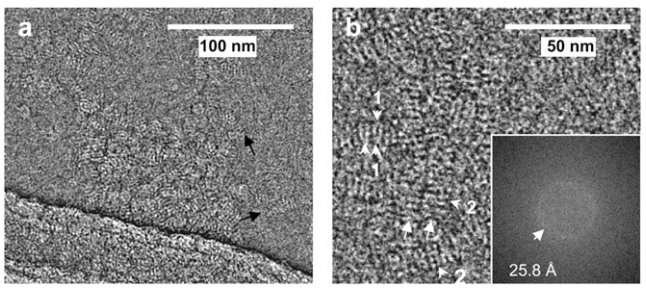

FIGURE 4 Mg^{2+}-NCP microaggregates formed at low starting NCP concentration (0.2 mg mL^{-1}) in the presence of 45 mM $MgCl_2$, and trapped in a thin film for cryoelectron microscopy. One aggregate ~150 nm in diameter is seen at low magnification (*a*). Higher magnification (*b*) allowed us to recognize a few columns partially aligned in parallel (*arrows*). The successive NCPs stacked in the columns present different orientations, as seen from the ''V'' shapes (*1*), two parallel strands (*2*), and intermediate patterns drawn by DNA that correspond to different side-view projections. Fourier transform of *b*, assessed by Image J, reveals a 25.8-Å periodicity.

X-ray diffraction spectra were recorded in various conditions in the phase diagram for starting NCP concentrations >5 mg mL^{-1}. Indeed, x-ray diffraction experiments require ~3 μL volumes of aggregates that we were not able to collect for the lowest concentrations. The spectra display very few organized states and are highly dependent on the equilibration time. After 1 month equilibration, the x-ray diffraction diagrams are characteristic of aggregated NCPs, whereas after 1 year of equilibration, a broad peak appears around $q \approx 0.12$ $Å^{-1}$, characterized by the stacking of NCPs into short columns. In nearly all conditions, the majority of spectra do not present Bragg peaks, indicating that there is no long-range order in those samples. Diffraction spectra are typical of NCPs either aggregated or piled up into small and irregular columns. For NCPs with starting concentration of 50 mg mL^{-1} and containing 20 mM Mg^{2+}, two peaks, indexed as 001 and 002, represent the first- and second-order columnar stacking, respectively (data not shown). From this indexation, the interparticle distance inside columns can be assessed as ~60 Å. From the width of the Bragg Peaks, it is estimated that this organization extends over ~40 particles. The low intensity of these peaks indicates that the ordering is restricted to small domains that coexist with unorganized domains. No other peak representative of any organization between columns is detected.

Spd^{3+}-NCP aggregates

For several starting NCP concentrations (6, 14, 20, 30, 40, 60, 100, 150, 200, and 240 mg mL^{-1}), NCPs were aggregated with varying amounts of Spd^{3+}. The structure of these aggregates was analyzed using optical microscopy and x-ray diffraction. Results obtained at 14 mg mL^{-1} will first be precisely described.

Spd^{3+}-NCP samples were introduced in flat glass capillaries immediately after vortexing and allowed to stabilize for times ranging from 1 month to 1 year. They were studied using either Nomarski DIC contrast or polarizing microscopy. Macroscopic phase separation is observed, similar to that shown in Fig. 3 *a*. Using a very low spermidine concentration (3 mM), hexagonal crystalline germs are seen (Fig. 5 *a*). As they grow, they appear to be formed of six individualized domains. Such germs coexist with both a dense isotropic phase and the dilute isotropic supernatant. These helical germs range from 10 to 20 μm in diameter. When aligned in the preparation plane, the germs are birefringent. The use of a λ plate shows that NCP columns are parallel to the elongation of the crystal (DNA molecules perpendicular

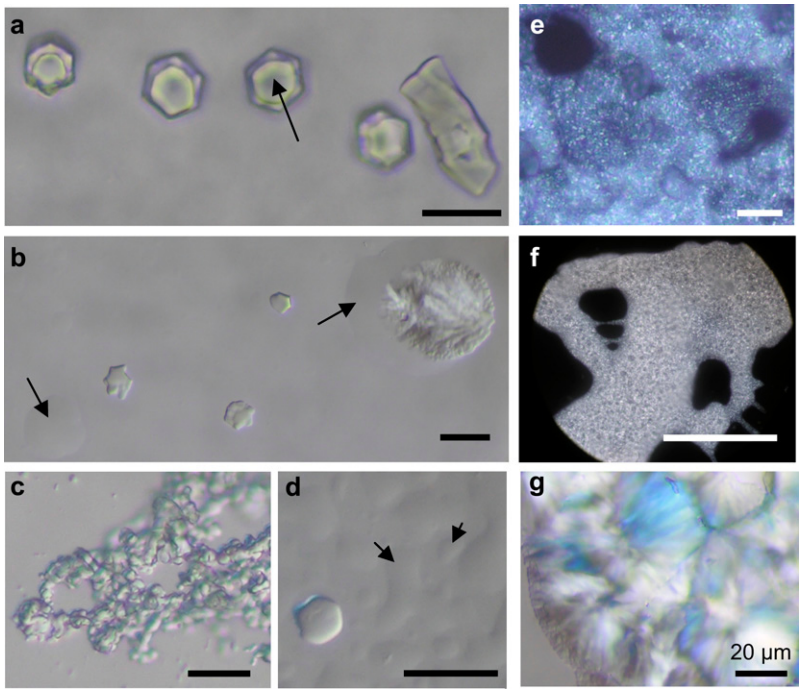

FIGURE 5 Spd^{3+}-NCP aggregates prepared with starting NCP concentrations of 14 mg/ml and various spermidine concentrations: 3 mM (*a*), 5 mM (*c*), 8 mM (*e*), 10 mM (*f*), 12.5 mM (*b* and *g*), 20 mM (*d*). Under favorable orientations, isolated hexagonal helicoidal crystals appear illuminated between crossed polars. They coexist with a dense isotropic solution that sticks them to the surface (*a*, *arrow*), keeps them together in a macroscopic fluid aggregate (*c*, *e*, and *f*), or flows around the crystals and dense parts of the aggregates (*b*, *arrows*). (*d*) This fluid, dense isotropic solution represents the major part of the aggregate and can be differentiated from the dilute isotropic solution (*arrows*). Only a few hexagonal aggregates can be seen, with limits that are not as sharp as in *a*. Observations are made in optical microscopy, with Nomarski DIC contrast (*a–d*) or between crossed polars (*e–g*). Scale bars, 20 μm.

to the axis of the crystal). Observing these hexagonal germs from above, no birefringence is detected between crossed polarizer and analyzer, confirming that NCP columns are oriented parallel to the optical axis of the microscope. With increasing spermidine concentrations (5, 8, 10, and 12.5 mM), Spd^{3+}-NCP aggregates are much larger and heterogeneous (Fig. 5, *b*, *c*, and *e–g*). They result from the aggregation of small birefringent crystallites glued together with a viscous isotropic and dense solution. For higher multivalent cation concentrations (20 mM Spd^{3+}), the samples are no longer birefringent (Fig. 5 *d*). However, phase separation is still visible with high-density isotropic droplets sedimented on the slide plane (Fig. 5 *d*, *arrows*).

X-ray diffraction was also performed on samples prepared at a 14 mg mL^{-1} NCP starting concentration, for Spd^{3+} concentrations varying from 7 to 50 mM (Fig. 6 *a*). Diffraction spectra change with spermidine concentration. At 7, 20, 30, and 40 mM Spd^{3+}, two broad peaks around 0.06 $Å^{-1}$ and 0.11 $Å^{-1}$ are observed, corresponding to distances of ~110 and 60 Å. Considering the NCP dimensions, the first peak (~0.06 $Å^{-1}$) corresponds to lateral spacing between NCPs. The second peak (~0.11 $Å^{-1}$) is mainly related to the first order of the NCP longitudinal stacking period and certainly encloses, to a minor extent, the lateral second-order interaction peak as well. At 50 mM Spd^{3+}, the diffraction spectra are representative of aggregated and unorganized NCPs. Sharp Bragg peaks are only obtained for 10 mM spermidine. Those peaks can be positioned at q_1, $q_1\sqrt{3}$, $q_1\sqrt{4}$, and $q_1\sqrt{7}$, and are therefore representative of a columnar hexagonal organization. A hexagonal parameter, a_H, equal to $2/\sqrt{3} \times 2\pi/q_1 = 114.3$ Å can be assessed. The peak width (full width at half-maximum) of 0.0015 $Å^{-1}$ is comparable to experimental resolution. The long-range ordering consequently extends over at least 3 μm. No other peaks are distinguished, characterizing the longitudinal order within columns. Either the longitudinal organization might be disordered or related peaks might be hidden by the other peaks. The well ordered organization was found to be precisely localized in the capillaries. X-ray diffraction patterns recorded a few millimeters away display Bragg peaks at identical positions, but with lower intensity, superimposed onto two broad peaks located around 0.06 $Å^{-1}$ and 0.11 $Å^{-1}$. These broad peaks are characteristic of the isotropic phase of irregular columns.

To analyze broad peaks more accurately and quantitatively, the scattering intensities, $I(q)$, were divided by the form factor of an isolated NCP (Fig. 6 *b*). The resulting structure factors, $S(q)$, display two major peaks that characterize 1), lateral ordering in the columnar two-dimensional (2D) hexagonal lattice, and 2), longitudinal ordering within columns. Both peaks were simultaneously fitted by the sum of the two following Lorentzian functions centered at q_1 and q_2, respectively:

The q_1 values are related to the lateral interparticle distances, a, between NCPs. The value of a depends on the type of organization, which is unknown. For a liquid ordering, a_L would equal $1.23 \times 2\pi/q_1$, and for a quasihexagonal ordering, a_H would equal $2\pi/q_1 \times 2/\sqrt{3}$. Assuming that the second peak is mainly due to the stacking of NCPs, q_2 is related to the distance, d, between two successive particles in the NCP columnar stacking ($d = 2\pi/q_2$). The NCP

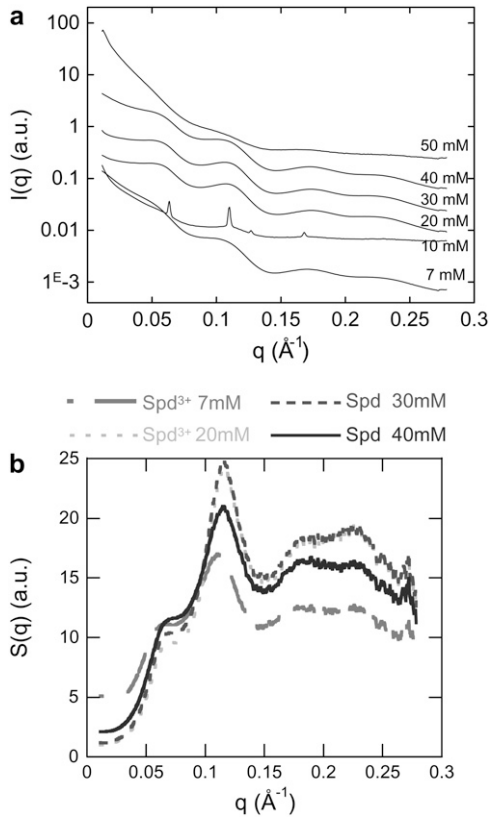

FIGURE 6 (*a*) Diffraction diagrams obtained for various spermidine concentrations ranging from 7 to 50 mM at a constant starting NCP concentration (14 mg mL^{-1}). Bragg peaks characterizing a hexagonal organization are obtained for a Spd^{3+} concentration of 10 mM. For any other conditions, broad peaks are observed. (*b*) Structure factors obtained after dividing the scattering intensity, $I(q)$, at 14 mg mL^{-1} by the form factor of the isolated NCPs.

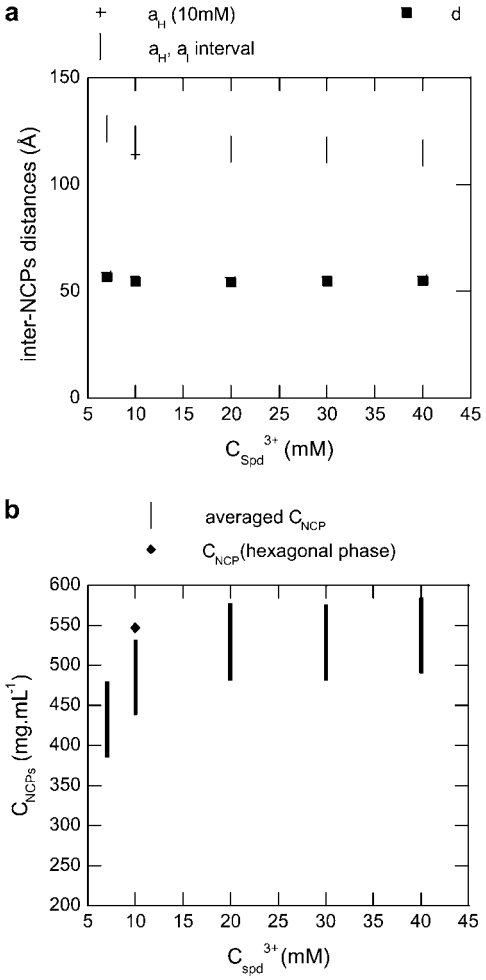

FIGURE 7 (*a*) Nucleosomal interdistances within Spd^{3+}-NCP aggregates with a starting NCP concentration of 14 mg mL^{-1} with various spermidine concentrations. d, distance between NCPs within columnar stacks; a_H and a_L, lateral distances within either a hexagonal or a liquid organization. Those distances were assessed from x-ray diffraction experiments. (*b*) Nucleosomal concentrations within Spd^{3+}-NCP aggregates with a starting NCP concentration of 14 mg mL^{-1}, at various spermidine concentrations.

concentration inside Spd^{3+}-NCP precipitates can be estimated using the previous parameters:

$$\frac{M}{Nad^2a_L^2\frac{\sqrt{3}}{2}} \le C_{NCPs} \le \frac{M}{Nad^2a_H^2\frac{\sqrt{3}}{2}}.$$

The width of the two broad peaks shown in Fig. 6 *b* evolves with spermidine concentration. It decreases from 7 to 10 mM Spd^{3+} (where Bragg peaks can be observed), then increases with higher Spd^{3+} concentrations, implying a disorder increase in the precipitate. This evolution tends to demonstrate that when the spermidine concentration is increased up to 10 mM, NCPs pile up on top of one another to form columns and a hexagonal lateral columnar ordering takes place simultaneously. Disorder also occurs simultaneously in the lateral and longitudinal directions when spermidine concentration is increased above 10 mM. Interparticle distances, as well as NCP concentrations, inside the precipitate were determined and the values are displayed in Fig. 7. The distance, d, between NCPs within columns varies only slightly with Spd^{3+} concentration, and is ~55 Å, independent of the multivalent salt concentration. The lateral distance between NCPs, in the a_H-a_L interval, ranges between 113 and 120 Å. The average final NCP concentration inside the precipitate is minimal at 7 mM Spd^{3+} and equal to 430 ± 35 mg mL^{-1}. This value further increases and plateaus at 530 ± 35 mg mL^{-1} for higher Spd^{3+} concentrations.

For any other NCP concentrations (data not shown), the NCP organization as a function of Spd^{3+} concentration follows the evolution detailed above at 14 mg mL^{-1}. The phase diagram presented in Fig. 8 features a recapitulative description of the various structural organizations obtained in Spd^{3+}-NCP aggregates. Optical microscopy, freeze-fracture electron microscopy, cryoelectron microscopy on thin film, and x-ray diffraction produce a set of complementary and concordant information, allowing us to describe the NCP

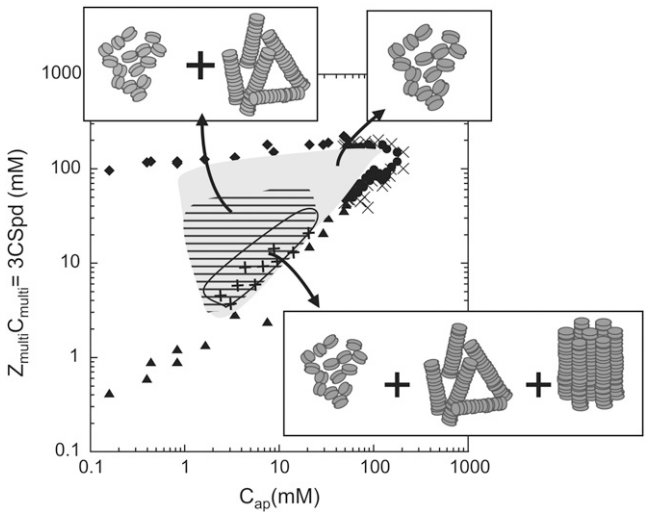

FIGURE 8 Structures of NCPs aggregated by spermidine and their localization in the phase diagram. The region where $C_{ap} < 1$ mg/ml was not fully explored. Symbols are the same as in Fig. 2.

dense-phase organization inside a large domain of NCP precipitation.

For any starting NCP concentrations with 10 mM $< C_{ap} <$ 50 mM, NCP aggregate organization changes with Spd^{3+} concentration along vertical lines in the phase diagram:

1. For the lowest Spd^{3+} concentrations, just above the precipitation limit, hexagonal crystallites are observed by optical microscopy. These crystallites coexist with a dense isotropic NCP solution that corresponds to a solution of columns or of isolated NCPs or both. The crystallites themselves represent only a few percent of the total NCP amount. After centrifugation in cylindrical capillaries, these small ($\sim$10 μm) germs are expected to fall down to the very bottom of the capillaries, which makes them inaccessible to x-rays.
2. For higher spermidine concentrations, optical microscopy demonstrates large fluid domains with many small birefringent dots. Diffraction diagrams display Bragg peaks characteristic of a hexagonal 2D organization in coexistence with a less ordered phase. In addition to prompting NCP top-to-bottom longitudinal interactions, spermidine is able to induce lateral NCP contacts as well. NCP columns get hexagonally packed, as already reported (17).
3. For additional amounts of spermidine ($Z_{multi}C_{multi} > 5C_{ap}$), hexagonal organization gets disrupted. Disordered columns and aggregated isolated NCP phases are obtained instead. With more than five positive charges available per negative charge on NCPs, there is a significant excess of spermidine in the precipitate. In conclusion, we observed that precipitates are well organized close to the precipitation threshold, whereas they are poorly structured along the redissolution threshold.

DISCUSSION

Polyelectrolyte-like behavior

Precipitation threshold

Precipitation occurs over the same range of NCP concentrations for both cations. Nevertheless, the biphasic region extends over a larger range for spermidine than magnesium.

The phase diagrams of NCPs precipitated with magnesium or spermidine display features common to colloid and polyelectrolyte solutions. Experimentally, similar behaviors have been described for polystyrene sulfonate, DNA, NCPs, and chromatin (11,19–21) displaying three distinct regimes of precipitation:

1. For the lowest NCP concentrations, the precipitation threshold seems rather constant. This regime is clearly visible for NCPs precipitated with magnesium for $C_{ap} <$ 5 mM and, to a lesser extent, with spermidine for $C_{ap} <$ 1 mM. For the latter, it would have been necessary to perform experiments using lower starting NCP concentrations to ascertain the existence of this regime. Unfortunately, experiments are precluded in this lower regime because NCPs are not stable at low concentration, and DNA gets dissociated from the histone core. In this region, the precipitation threshold depends on multiple parameters, as the ion valence or the added monovalent salt (19). Increasing the amount of monovalent salt in the solution induces a decrease in the fraction of precipitated NCPs (data not shown). We suspect that the fraction of monovalent ions bound to NCPs gets higher and competes with multivalent ions for binding to NCPs. Consequently, precipitation is altered. In this regime, the precipitation of NCPs requires lower spermidine charges than magnesium charges, as expected theoretically (22, 23). Since the precipitation threshold is above the electroneutrality line (Fig. 2, *a* and *b*), a multivalent counterion fraction is free in solution. This result is in agreement with polyelectrolyte theories since, according to Rouzina and Bloomfield (22) and Grosberg and co-workers (24), precipitation occurs for $(Z_{multi}e)^2/\varepsilon a_z k_B T \geq 2$, where e is the elementary charge, ε the dielectric constant, a_z the distance between condensed ions and k_BT the thermal energy.
2. For higher starting NCP concentrations (5 mM $< C_{ap} <$ 40 mM for magnesium and 1 $< C_{ap} <$ 90 mM for spermidine), the precipitation line is independent of the precipitating agent and is superimposed to the electroneutrality line, $Z_{multi}C_{prec} \approx C_{ap}$. Precipitation occurs when the number of positive charges carried by cations equals the number of negative charges available on NCPs. In such conditions, all multivalent cations are therefore bound to NCPs.
3. For the highest NCP concentrations ($C_{ap} >$ 40 mM for Mg^{2+} and $C_{ap} >$ 90 mM for Spd^{3+}), the precipitation line is slightly below the electroneutrality line. As $Z_{multi}C_{precip} < C_{ap}$, polycations are partly bound to the

NCPs and partly free in solution. This phenomenon is better seen in the NCP-Mg^{2+} phase diagram, where the slope of the precipitation line seems to be small (for 40 mM $< C_{ap} <$ 80 mM), suggesting that the number of polycations per NCP necessary to induce aggregation is lower for $C_{ap} = 80$ mM than for $C_{ap} = 40$ mM. This slope gets steeper for higher concentrations.

Redissolution threshold

In both phase diagrams considered in this work, redissolution was observed above certain multivalent cation concentrations. The redissolution thresholds of NCP precipitated with either magnesium or spermidine are nearly identical for $C_{ap} <$ 10 mM. The redissolution threshold increases slowly and linearly with the NCP concentration. For Spd^{3+}, the same behavior is observed at higher NCP concentrations. On the contrary, the redissolution threshold increases sharply to $C_{ap} \approx 40$ mM for NCPs precipitated with magnesium.

Numerous theories describe precipitation of charged colloids or polyelectrolytes induced by multivalent ions of opposite charge. Different mechanisms were suggested to explain the reemergence of a soluble phase:

1. Correlation between counterions can lead to an overcharging effect that renders DNA positively charged and therefore increases the repulsion between particles (22,23).
2. An ion bridging model has also been proposed. In this model, simple screening would reduce all the electrostatic interactions, in particular the attractive ones, thus leading to a solubilization of the particles (25).
3. ''Ion pairing'' or association of co-ions would reduce the effective charge of the counterions and could consequently reduce the condensation effect (26). In our system, Mg^{2+}-NCP aggregates stay negatively charged and are not overcharged (11). Therefore, simple screening and ''ion pairing'' could be the dominant effects involved in redissolution. In contrast, a small charge inversion has been observed for Spd^{3+}-NCP aggregates (11); in this case, all three phenomena could play a role.

A complete phase diagram of NCPs precipitated using magnesium has been described by de Frutos et al. (11). The only discrepancy is seen along the redissolution line, where the increase above $C_{ap} = 10$ mM is more significant in this work. This could be due to the slightly different experimental conditions used by de Frutos et al. In their experiments, the monovalent salt concentration was lower (3.5 mM instead of 10 mM) and EDTA was present. As a chelator of divalent ions involved in enzymatic activities of DNase or proteases, EDTA is commonly used in all buffers. But EDTA is not found in vivo. In this work, we wanted to avoid this chelating effect to get closer to physiological conditions. For this reason, all the experiments were made in the absence of EDTA, and we carefully guarded against DNA or protein degradation. EDTA, which was present in the de Frutos et al. experiments, might have been in competition with NCPs for Mg^{2+}, and would be responsible for this shrinking.

Closure of the phase diagrams

At the highest particle and ionic concentrations, NCPs stay soluble. For both phase diagrams, the domain where NCPs are aggregated is apparently closed at high NCP and multivalent cation concentrations. Considering polyelecrolytes precipitated by multivalent cations, theoretical approaches predict an opening of the phase diagram with a thin chimney extending toward the highest polyelectrolyte and cation concentrations (27). Since this domain may be narrow and difficult to locate, a large series of experimental points were made. Owing to our insistent exploration of this region, we can ascertain that this ''chimney'' is extremely reduced, if it exists at all. To our knowledge, no experimental data have been collected yet in this region with polylectrolytes or charged colloids, which can be understood by the difficulty of exploring this region of extreme concentrations.

Maximum of precipitation

The precipitation maxima of the two diagrams are significantly different. For low C_{ap}, this maximum of precipitation occurs over a wide range of Spd^{3+} concentrations. This range is gradually reduced when the NCP concentration is increased. This behavior seems to be independent of the polyelectrolyte, as it was already observed for short DNA fragments (150 bp) and long DNA chains (λ and T4 DNA) precipitated with spermidine (19). The same effect was also found for one fixed λ DNA concentration (50 ng/ml) when increasing the monovalent salt concentation. The range of maximum precipitation was two times smaller at high monovalent salt concentration (100 mM) than at low salt (10 mM) (28). Since 100 mg mL^{-1} of NCPs ($C_{ap} = 79$ mM) brings 75 mM of monovalent counterions, one can argue that the reduction of the precipitation maximum could be related to the increase of counterions in the solution.

This argument is no more valid for NCPs precipitated with magnesium, for which the phenomenon is inverted. For NCPs precipitated with magnesium, the maximum of precipitation occurs for one precise Mg^{2+} concentration for low C_{ap}, whereas it takes place on a large range of magnesium concentrations where C_{ap} is increased. It would be interesting to clarify whether this difference arises from the valence, from the steric issues of the condensing agents, or from specific interactions between NCPs and Mg^{2+} and/or Spd^{3+}.

The structure of dense NCP phases

NCP-Spd^{3+} aggregates and their localization in the phase diagram

We have shown here how the organization of DNA in the precipitate highly depends on the conditions of precipitation. Precipitates are highly ordered close to the precipitation line,

and progressively disorganized when either the concentration of spermidine or the concentration of NCPs is increased. For the highest NCP concentrations ($C_{ap} > 50$ mM), NCP aggregates are isotropic. These can be aggregates of NCPs or aggregates of NCPs stacked in columns. We have shown how variations of ionic conditions can mediate the degree of compaction of the NCPs. Indeed, monovalent counterions initially bound to NCPs are released in solution upon exchange with multivalent cations. For high initial NCP concentrations, monovalent ionic concentrations may become significantly high. These ions are likely to screen attractive interactions induced by condensed spermidine and to prevent any ordering in the aggregates. The same phenomenon has already been observed and analyzed in detail for short DNA molecules precipitated with spermidine (29). The spacing between two DNA molecules in the precipitate was found to increase with spermidine concentration and also with counterion concentration. Close to the resolubilization line, the DNA aggregates were isotropic as well.

NCP-magnesium aggregate organization

Magnesium is also able to condense NCPs into dense precipitates. This result has been theoretically predicted by Korolev et al. (30) using a coarse-grained model where the NCP is modeled as a negatively charged spherical particle with flexible polycationic histone tails attached to it. In the presence of $MgCl_2$, the NCPs aggregate via histone-tail bridging and accumulation of counterions. No order is observed inside these aggregates, probably due to the fact that the geometry of the NCP is not taken into account in their model. Nevertheless, the Mg^{2+}-NCP aggregates observed here are poorly organized. In the more favorable conditions, NCPs form a columnar phase, where columns are irregular and uncorrelated one to another. As for spermidine, the only partially and locally organized precipitates are obtained for the lowest magnesium concentrations tested, close to the precipitation threshold. Magnesium favors NCP longitudinal top-to-bottom interactions, but we did not observe any lateral correlation between columns using x-ray diffraction and cryoelectron microscopy. A lower valence, as compared with Spd^{3+}, seems to disfavor a long-range organization of NCPs.

Ordering of NCPs in precipitated phases

Under conditions of precipitation, NCPs display a wide variety of organizations. A dense isotropic phase of isolated NCPs, a dense phase of disordered columns, and a 2D columnar hexagonal phase have been observed in the precipitate for NCPs aggregated with spermidine. The data presented here may be considered a catalog of the possible ways NCPs organize in the presence of divalent or trivalent ions and their preferential modes of interaction. Nevertheless, the organization of NCPs in different phases, or the boundaries of these phases within the phase diagrams, may slightly depend on the DNA length associated with the histone octamer and its polydispersity. In this work, this length was equal to 155 ± 20 basepairs. More ordered phases may be present with perfectly monodisperse NCPs.

In a previous study of NCPs precipitated with spermidine, Leforestier and co-workers (17) described a columnar organization. They also observed a flow-induced nematic phase by optical microscopy, after centrifugation of their samples up to $11{,}000 \times g$. In this work, we found that NCPs pile up into columns with either weak (columnar phases) or strong (hexagonal or quasihexagonal phases) lateral interactions between columns. It is possible that this disordered columnar phase corresponds to the nematic phase previously observed.

Comparison with condensed phases in the presence of monovalent salt

The lamellocolumnar phase and the inverse hexagonal phase described previously in the presence of monovalent salts only (8) were not found here. These two dense ordered phases were formed under low monovalent salt conditions. The high NCP concentration was reached by applying an osmotic pressure using a stressing polymer (polyethylene glycol) (31) or by elimination of the buffer, since monovalent ions do not induce aggregation of NCPs. These two structures also rely on the formation of columns of stacked NCPs, but NCPs are rotationally oriented in the columns. The two structures are stabilized by short-range lateral attractive interactions between NCPs that maintain the bilayer structure locally, and by long-range repulsive interactions between the bilayers. In this work, interactions between NCPs are mainly governed by short-range attraction between NCPs. The long-range repulsions between NCPs are screened by Mg^{2+} or Spd^{3+} ions. Therefore the emergence of these two phases is prevented.

Interestingly, the hexagonal columnar organization is obtained under all ionic conditions that have been tested, in the presence of mono-, di-, and trivalent cations. In the presence of monovalent salt exclusively (25–100 mM), NCP concentration was shown to exceed 450 mg mL^{-1} (7), which is in the concentration range reported here (450–560 mg mL^{-1}; Fig. 7).

Generalization to chromatine/chromosomes

Several experimental (9,10) and theoretical (32,33) studies have focused on chromosome and chromatin chain condensation induced by monovalent and multivalent cations.

Poirier et al. (9) showed how chromosomes can follow a condensation-decondensation process upon addition of multivalent cations. With magnesium concentrations varying from 10 to 100 mM, chromosomes are fully condensed. In that magnesium concentration range, NCPs are also condensed for starting NCP concentration >50 mg/ml (Fig. 2 *a*). Interestingly, the lowest in vivo NCP concentrations are always >50 mg mL^{-1}, even in the interphase chromosome.

Widom (10) has shown that chromatin containing linker histones precipitates for magnesium concentrations exceeding

0.5 mM in the presence of 10 mM monovalent salt. We recall that isolated NCPs do not precipitate under these conditions. Chromatin free of linker histones precipitates above 2 mM divalent salt in the presence of 10 mM monovalent salt and is resolubilized above 60 mM divalent salt concentration (10). These results, using 12-mer oligonucleosomes, are comparable to those observed for isolated NCPs (155 $\pm$ 20 bp here). Thus, linker histones facilitate chromatin condensation (10). Linker histones are actually very basic and partially neutralize the NCP negative charge. Electrostatic repulsions within chromatin are partially screened and chromatin precipitation therefore requires lower quantities of multivalent ions. It has also been shown that histone tails play a crucial role in chromatin folding (34). Finally, it appears that chromatin condensation results from a delicate balance between electrostatic interactions involving histone tails, linker DNA, and linker histones.

This hypothesis has been well described theoretically by Schlick and co-workers using computer simulation on nucleosomal arrays (32,33). A model has been designed in which the NCP and linker DNA are represented using a discrete surface-charge optimization model, which treats the NCP and the linker DNA as an electrostatic surface symbolized by a few hundred effective charges; the histone tails are modeled using a chain hydrodynamic approach. Interestingly, the energy analyses indicate that the repulsion among linker DNAs leads to an extended form of nucleosomal array, whereas internucleosome attractions mediate the folding at high monovalent salt concentrations. The balance between these two contributions is mediated by histone tails and regulates the salt-dependent condensation of chromatin. It would be interesting to study aggregation of multivalent cations using this model.

CONCLUSION

We have performed a systematic study to build phase diagrams for NCPs precipitated by divalent (magnesium) and trivalent (spermidine) cations. In those phase diagrams, the structures of the aggregates were analyzed in detail to display internucleosomal preferential interaction modes. Within the nuclear concentration range (35), multivalent ions may induce NCP precipitation and lead to NCP concentrations similar to those found in vivo (50–500 mg mL^{-1}). We previously built a phase diagram of NCPs in the presence of monovalent ions exclusively. A library of high-density NCP phase structures is now available for salts of various valence. Very locally, chromatin could feature similar structural patterns. We intend to concentrate future investigations on testing that hypothesis.

This work greatly benefited from stimulating discussions with Eric Raspaud. We are very grateful to Stephanie Finet for assistance in using beamline ID2 at the European Synchrotron Radiation Facility. We also thank the referees whose comments helped us to improve this article.

This research was supported by ANR blanche CNRS/USAR (ANR-06-BLAN-0195).

REFERENCES

1. Luger, K., A. W. Mader, R. K. Richmond, D. F. Sargent, and T. J. Richmond. 1997. Crystal structure of the nucleosome core particle at 2.8 Å resolution. *Nature*. 389:251–260.
2. Davey, C. A., D. F. Sargent, K. Luger, A. W. Maeder, and T. J. Richmond. 2002. Solvent mediated interactions in the structure of the nucleosome core particle at 1.9 Å resolution. *J. Mol. Biol.* 319:1097–1113.
3. de Vries, R., and M. C. Stuart. 2006. Theory and simulations of macroion complexation. *Curr. Opin. Colloid Interface Sci.* 11:295–301.
4. van der Kooij, F. M., K. Kassapidou, and H. N. W. Lekkerkerker. 2000. Liquid crystal phase transitions in suspensions of polydisperse plate-like particles. *Nature*. 406:868–871.
5. Bouyer, F., A. Robben, W. L. Yu, and M. Borkovec. 2001. Aggregation of colloidal particles in the presence of oppositely charged polyelectrolytes: effect of surface charge heterogeneities. *Langmuir*. 17:5225–5231.
6. Candia, J. 2006. Irreversible growth of binary mixtures on small-world networks. *Phys. Rev. E.* 74:031101.
7. Mangenot, S., A. Leforestier, D. Durand, and F. Livolant. 2003. Phase diagram of nucleosome core particles. *J. Mol. Biol.* 333:907–916.
8. Livolant, F., S. Mangenot, A. Leforestier, A. Bertin, M. De Frutos, E. Raspaud, and D. Durand. 2006. Are liquid crystalline properties of nucleosomes involved in chromosome structure and dynamics? *Philos. Transact. A.* 364:2615–2633.
9. Poirier, M. G., T. Monhait, and J. F. Marko. 2002. Reversible hypercondensation and decondensation of mitotic chromosomes studied using combined chemical-micromechanical techniques. *J. Cell. Biochem.* 85:422–434.
10. Widom, J. 1986. Physicochemical studies of the folding of the 100 Å nucleosome filament into the 300 Å filament. Cation dependence. *J. Mol. Biol.* 190:411–424.
11. de Frutos, M., E. Raspaud, A. Leforestier, and F. Livolant. 2001. Aggregation of nucleosomes by divalent cations. *Biophys. J.* 81:1127–1132.
12. Bloomfield, V. A., C. L. Ma, and P. G. Arscott. 1994. Role of multivalent cations in condensation of DNA. *In* Macro-Ion Characterization. American Chemical Society, Washington. 195–209.
13. Tabor, C. W., and H. Tabor. 1984. Polyamines. *Annu. Rev. Biochem.* 53:749–790.
14. Davis, R. H., D. R. Morris, and P. Coffino. 1992. Sequestered end-products and enzyme regulation. The case of ornithine decarboxylase. *Microbiol. Rev.* 56:280–290.
15. Strick, R., P. L. Strissel, K. Gavrilov, and R. Levi-Setti. 2001. Cation-chromatin binding as shown by ion microscopy is essential for the structural integrity of chromosomes. *J. Cell Biol.* 155:899–910.
16. Watanabe, S., K. Kusamaeguchi, H. Kobayashi, and K. Igarashi. 1991. Estimation of polyamine binding to macromolecules and ATP in bovine lymphocytes and rat liver. *J. Biol. Chem.* 266:20803–20809.
17. Leforestier, A., S. Fudaley, and F. Livolant. 1999. Spermidine-induced aggregation of nucleosome core particles: evidence for multiple liquid crystalline phases. *J. Mol. Biol.* 290:481–494.
18. Mangenot, S., A. Leforestier, P. Vachette, D. Durand, and F. Livolant. 2002. Salt-induced conformation and interaction changes of nucleosome core particles. *Biophys. J.* 82:345–356.
19. Raspaud, E., M. O. de la Cruz, J. L. Sikorav, and F. Livolant. 1998. Precipitation of DNA by polyamines: a polyelectrolyte behavior. *Biophys. J.* 74:381–393.
20. Raspaud, E., I. Chaperon, A. Leforestier, and F. Livolant. 1999. Spermine-induced aggregation of DNA, nucleosome, and chromatin. *Biophys. J.* 77:1547–1555.

21. Delsanti, M., J. P. Dalbiez, O. Spalla, L. Belloni, and M. Drifford. 1994. Phase-diagram of polyelectrolyte solutions in presence of multivalent salts. *In* Macro-Ion Characterization. American Chemical Society, Washington. 381–392.

22. Rouzina, I., and V. A. Bloomfield. 1996. Macroion attraction due to electrostatic correlation between screening counterions. 1. Mobile surface-adsorbed ions and diffuse ion cloud. *J. Phys. Chem.* 100:9977–9989.

23. Shklovskii, B. I. 1999. Screening of a macroion by multivalent ions: Correlation-induced inversion of charge. *Phys. Rev. E Stat.* 60:5802–5811.

24. Grosberg, A. Y., T. T. Nguyen, and B. I. Shklovskii. 2002. Colloquium: the physics of charge inversion in chemical and biological systems. *Rev. Mod. Phys.* 74:329–345.

25. Olvera de la Cruz, M., L. Belloni, M. Delsanti, J. P. Dalbiez, O. Spalla, and M. Drifford. 1995. Precipitation of highly-charged polyelectrolyte solutions in the presence of multivalent salts. *J. Chem. Phys.* 103: 5781–5791.

26. Solis, F. J. 2002. Phase diagram of dilute polyelectrolytes: collapse and redissolution by association of counterions and co-ions. *J. Chem. Phys.* 117:9009–9015.

27. Nguyen, T. T., and B. I. Shklovskii. 2001. Complexation of DNA with positive spheres: phase diagram of charge inversion and reentrant condensation. *J. Chem. Phys.* 115:7298–7308.

28. Jarry, D. 1998. Rheology of semidiluted and cyclization of globular chains. PhD thesis, University Paris-XI, Orsay, France.

29. Raspaud, E., D. Durand, and F. Livolant. 2005. Interhelical spacing in liquid crystalline spermine and spermidine-DNA precipitates. *Biophys. J.* 88:392–403.

30. Korolev, N., A. P. Lyubartsev, and L. Nordenskiold. 2006. Computer modeling demonstrates that electrostatic attraction of nucleosomal DNA is mediated by histone tails. *Biophys. J.* 90:4305–4316.

31. Rau, D. C., B. Lee, and V. A. Parsegian. 1984. Measurement of the repulsive force between polyelectrolyte molecules in ionic solution: hydration forces between parallel DNA double helices. *Proc. Natl. Acad. Sci. USA.* 81:2621–2625.

32. Arya, G., and T. Schlick. 2006. Role of histone tails in chromatin folding revealed by a mesoscopic oligonucleosome model. *Proc. Natl. Acad. Sci. USA.* 103:16236–16241.

33. Sun, J., Q. Zhang, and T. Schlick. 2005. Electrostatic mechanism of nucleosomal array folding revealed by computer simulation. *Proc. Natl. Acad. Sci. USA.* 102:8180–8185.

34. Dorigo, B., T. Schalch, K. Bystricky, and T. Richmond. 2003. Chromatin fiber folding: requirement for the histone H4 N-terminal tail. *J. Mol. Biol.* 327:85–96.

35. Bohrmann, B., M. Haider, and E. Kellenberger. 1993. Concentration evaluation of chromatin in unstained resin-embedded sections by means of low-dose ratio-contrast imaging in stem. *Ultramicroscopy.* 49:235–251.